POLITECNICO DI TORINO
Repository ISTITUZIONALE

Exploring lithium diffusion in LiF with machine learning potentials: from point defects to collective ring diffusion

Original
Exploring lithium diffusion in LiF with machine learning potentials: from point defects to collective ring diffusion / De Angelis, P., Raucci, U., Mambretti, F., Fasano, M., Chiavazzo, E., Asinari, P., Parrinello, M.. - In: NPJ COMPUTATIONAL MATERIALS. - ISSN 2057-3960. - ELETTRONICO. - 12:1(2026), pp. 1-12. [10.1038/s41524-026-02132-8]

Availability:
This version is available at: 11583/3012929 since: 2026-07-10T09:34:51Z

Publisher:
Nature Research

Published
DOI:10.1038/s41524-026-02132-8

Terms of use:

This article is made available under terms and conditions as specified in the corresponding bibliographic description in the repository

Publisher copyright

(Article begins on next page)

16 November 2026

npj | computational materials

Article

Published in partnership with the Shanghai Institute of Ceramics of the Chinese Academy of Sciences

https://doi.org/10.1038/s41524-026-02132-8

Exploring lithium diffusion in LiF with machine learning potentials: from point defects to collective ring diffusion

Check for updates

Paolo De Angelis[1,2] ✉, Umberto Raucci[1], Francesco Mambretti[1], Matteo Fasano[2], Eliodoro Chiavazzo[2,3], Pietro Asinari[2,3] & Michele Parrinello[1] ✉

Lithium fluoride (LiF) is a fundamental inorganic component of the solid electrolyte interphase (SEI) in lithium-ion batteries, yet its intrinsic ionic transport properties remain poorly understood, since there is a lack of direct experimental data, and standard computational approaches have difficulties in modeling these phenomena. Here, we train a machine learning based interatomic potential (MLIP) to perform large-scale Molecular Dynamics simulations of lithium diffusion in bulk LiF with near-DFT accuracy. Our study reveals not only conventional vacancy and interstitial transport mechanisms, but also a novel collective ring diffusion process involving six lithium ions. This mechanism arises under high interstitial concentrations, and it is stabilized by partial charge delocalization. Given the dynamic evolution of the SEI under electrochemical cycling, we suggest that such correlated diffusion events may be transiently active in LiF-rich regions. More broadly, our results demonstrate the power of MLIPs to access long timescales and complex dynamical behavior, providing a robust framework for future multiscale modeling of the SEI.

In the three decades since their first commercialization in 1991[1], lithium-ion batteries (LIBs) have become the dominant electrochemical energy storage technology, with widespread applications ranging from portable electronics to electric vehicles (EVs) and energy storage systems (ESSs)[2–4].

Regardless of the cell formats – coin, cylindrical (Fig. 1a), pouch, and prismatic cells – every LIB is formed by an anode, a cathode, an electrolyte (Fig. 1b) and auxiliary components such as separator, current collectors, and binders to store electrical energy in the form of chemical potential[1].

The widespread use of LIBs as ESSs is driving demand and development toward batteries that are more energy dense, eco-friendly, robust, and safe[5,6]. Despite significant progress over the past two decades, designing next-generation batteries remains hindered by our limited understanding of anode-electrolyte interfacial chemistry[7]. In this region, a nanometer-thick layer known as the solid electrolyte interphase (SEI) forms. The SEI results from the reduction reactions involving lithium ions and the organic electrolyte molecules at the anode surface[7,8]. This passivation layer insulates the anode while permitting the Li-ion transport and extending the electrolyte stability window, which is essential for efficient LIB function[7,8].

However, SEI's formation, stability, evolution, and ion transport mechanisms[9] are still not fully understood[4,7]. Because the SEI significantly governs cycling instability, resistance growth, and capacity fade[10–12], closing this knowledge gap is crucial to boost the efficiency and lifespan of next-generation LIBs[4,7,13].

Recent experiments have shown that[14–16] SEI consist of both inorganic and organic by-products of electrolyte reduction in a mosaic[17,18] or multi-layer structure[19,20] (Fig. 1c). The dense inorganic sub-layer of the SEI – typically a mixture of Li_2CO_3, Li_2O, and LiF – acts as the first electron-blocking barrier and dictates interphase durability[15,16]. Therefore, controlling and stabilizing the formation of this inorganic-rich inner layer is essential for producing a functional SEI[21]. Since LiF combines a wide band-gap (which helps block electron tunneling), high mechanical strength, and low solubility, recent work has shifted toward LiF-rich SEIs[22]. Several studies have indeed reported improvements in cycling stability, interfacial integrity, electrochemical performance, and flame resistance when the LiF content of the SEI is increased[23] via fluorine-rich electrolyte additives[24,25], fluorinated salts[26,27] or deposition[28–33].

At the same time, a central paradox remains: bulk LiF is a poor ionic conductor, yet LiF-rich interphases often correlate with better rate capability and stability. Recently, high-resolution spectroscopic experiments have begun to shed light on this conundrum, revealing that LiF in the SEI can form LiF-LiH solid solutions with enhanced ionic conductivity[34]. Moreover, LiF in the SEI can be amorphous or lattice-expanded relative to bulk LiF, implying structure and transport distinct from the bulk phase. This refined

[1]Laboratory of Atomistic Simulations, Italian Institute of Technology, Genova, Italy. [2]Department of Energy "Galileo Ferraris", Politecnico di Torino, Turin, Italy. [3]Istituto Nazionale di Ricerca Metrologica, Torino, Italy. ✉e-mail: paolo.deangelis@polito.it; michele.parrinello@iit.it

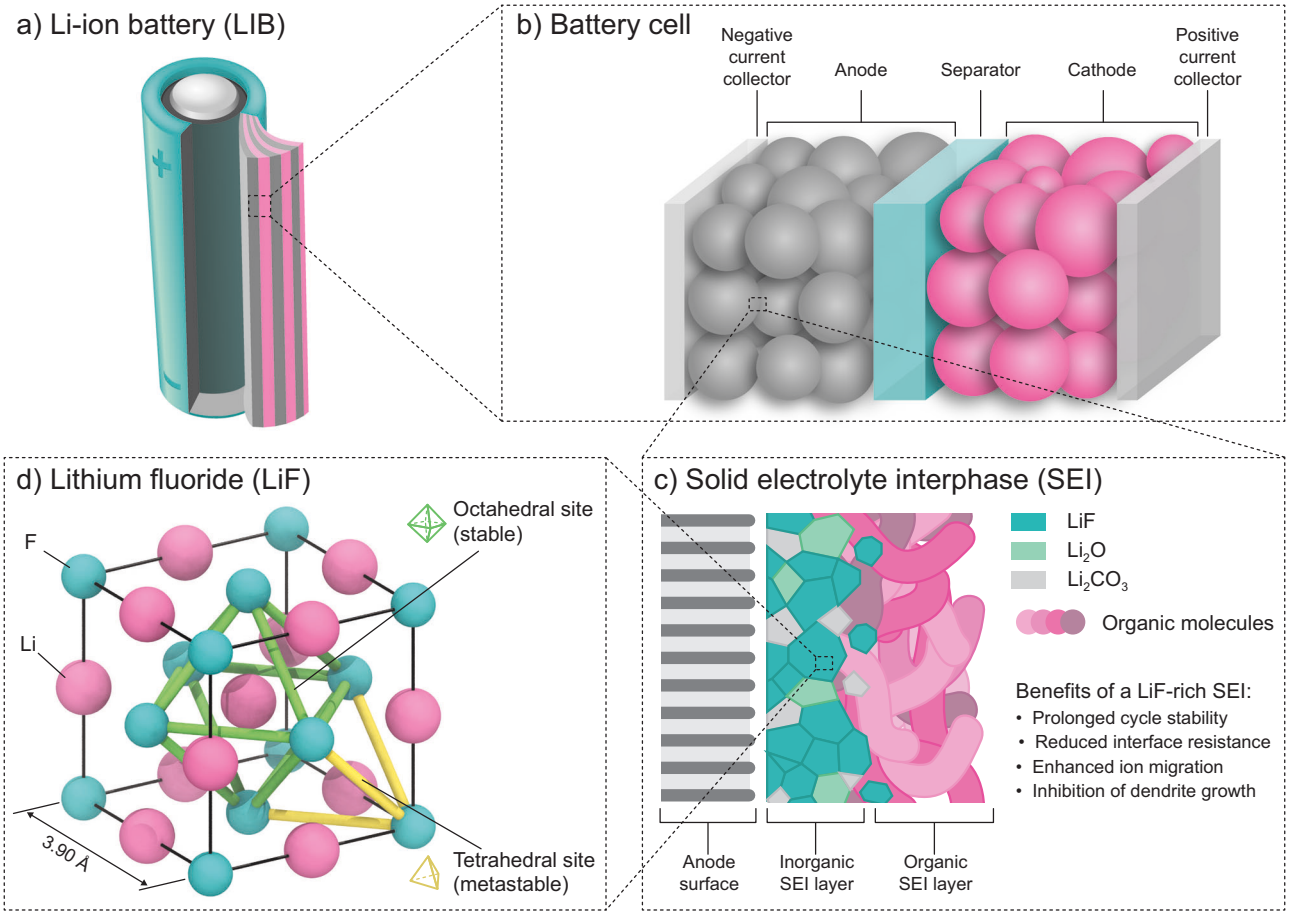


Fig. 1 | Multiscale nature of lithium-ion batteries. a Cylindrical LIB cell formed by a stratification of several cells (**b**) formed by two active materials – cathode and anode – and three auxiliary components – the two current collectors and the separator. On the surface of the anode active material particle (**c**), we have the formation of the solid electrolyte interface formed by inorganic salts (Li_2O, Li_2CO_3, LiF) and organic molecules (such as Lithium Ethylene Dicarbonate Li_2EDC, $C_4H_4Li_2O_6$), Lithium Methyl Carbonate (LMC, $C_2H_3LiO_3$). **d** Conventional unit cell of inorganic LiF, showing the octahedral and tetrahedral sites for lithium.

picture strengthens the need for a quantitatively reliable, atomistic description of Li^+ diffusion in LiF-rich environments.

Atomistic simulations, particularly molecular dynamics (MD), are uniquely suited to provide an atomistic picture of diffusion, capturing ion hops and correlated motion while enabling rigorous, statistical quantification. However, before simulating directly the multiphase SEI, a necessary first step is to characterize the Li^+ diffusion mechanism in bulk LiF, quantifying the dominant carriers (vacancies vs. interstitials), hop pathways, and activation energies. By pinning down LiF's intrinsic diffusion mechanisms, we can provide reference parameters to rationalize the behavior of LiF-rich SEI interphases. In this sense, the present bulk-LiF analysis serves as a mechanistic reference and limiting case for Li transport through LiF-rich SEI regions, rather than as a comprehensive model of ion conduction in the heterogeneous SEI. In realistic SEI morphologies, however, interfaces, grain boundaries, structural disorder, and non-bulk LiF environments may provide distinct transport pathways[35,36]. Therefore, understanding Li^+ diffusion in bulk LiF is a crucial initial step before modeling more complex SEI systems. Here, using state-of-the-art molecular dynamics powered by ab initio-quality machine-learning-based interatomic potentials, we perform long-time- and large-scale simulations, obtaining a close view of Li^+ dynamics in the LiF matrix and extracting detailed insights into the underlying diffusion mechanism.

Furthermore, we present an advanced local-environment descriptor-based analysis to characterize the coupled dynamics of interstitial atoms with their surroundings, thereby enhancing our understanding of diffusivity. Specifically, we compute the Smooth Overlap of Atomic Positions (SOAP) descriptor for every Li atom at each MD frame, yielding a rotation-invariant fingerprint of its coordination shell. This allows us (i) identifying which Li atoms are actively diffusing even when all Li are mobile, (ii) tracking and quantifying the atoms that participate in each hop, (iii) segmenting trajectories into lattice, transition, and interstitial regimes, (iv) extracting mechanistic insight along diffusion events. These analyses, combined with MLIP-driven MD at scale, hold promises for future investigation of Li-ion diffusion behavior in multicrystalline SEI.

Results

In this section, after testing the MLIP performance and its predictions for bulk LiF, we exploit the accuracy and speed-up offered by the MLIP to investigate lithium diffusion mechanisms.

Bulk phase characterization

Previous efforts to construct a reactive force field for LiF revealed significant challenges in reproducing the solid-phase characteristics of this SEI component at sub-melting temperatures (below 1121.35 K [37]). In particular, the common ReaxFF parameterization[38,39] used in SEI formation and growth studies tends to predict unstable LiF, which leads to amorphization, an artifact that hinders a proper description of crystalline stability. A recent study[40] introduced a refined ReaxFF parameterization that utilized tailored training configurations to mitigate the amorphization issue, resulting in improved structural stability. Nonetheless, even with these updates, discrepancies from ab initio reference data remained, indicating that further enhancements are necessary.

To overcome these limitations, we trained an MLIP for crystalline LiF that reproduces ab initio energetics and forces while enabling large-scale,

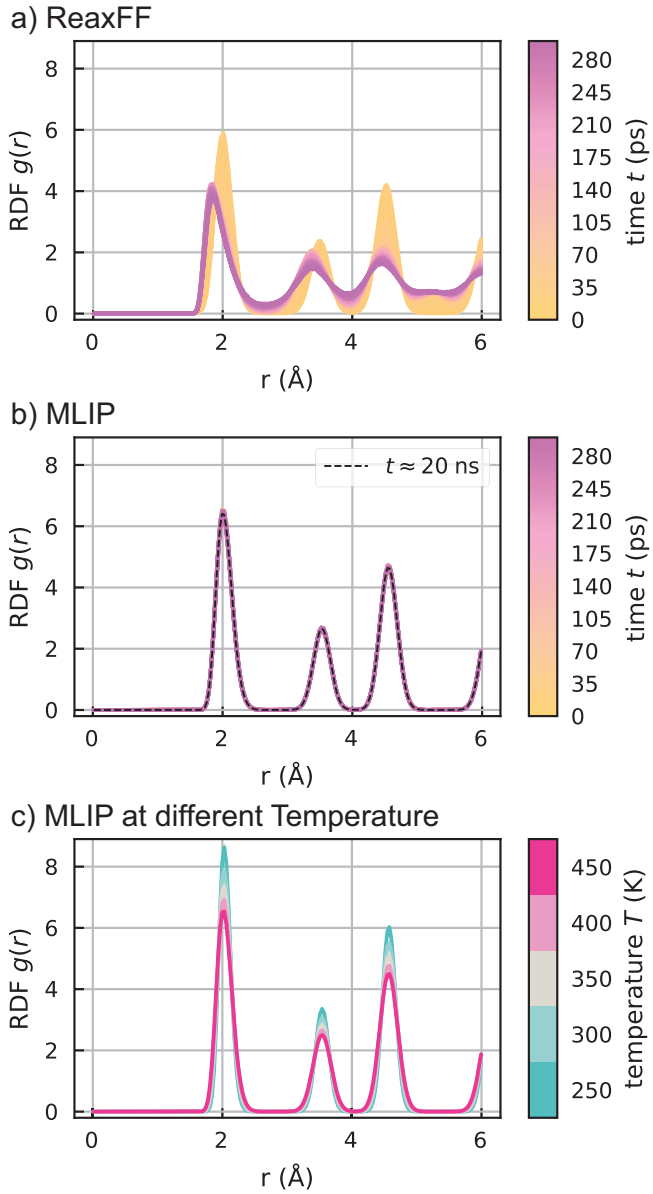


Fig. 2 | Li-F radial distribution function (RDF), $g(r)$, computed for two reactive force fields: a ReaxFF and b a ML-based interatomic potential (MLIP). The upper panels (**a**) and (**b**) show the time evolution of the RDF during the initial phase of the NVT simulations. Each curve represents the RDF averaged over 4 ps windows for the first 300 ps, colored according to the colormap on the right; in (**b**), the average RDF after ≈20 ns is also shown as a dashed line. **c** shows the temperature dependence of the RDF, obtained by averaging RDFs from four 20 ns replicas of each NVT simulation at 250 K, 300 K, 350 K, 400 K, and 450 K. The average RDFs are plotted with colors corresponding to each temperature (right colormap); shaded areas denote confidence intervals (not visible as they are smaller than the line thickness).

long-time simulations. As the first benchmark of this MLIP, we compare the crystal structure properties prediction against the recent ReaxFF. We consider the stable face-centered cubic (FCC) LiF structure illustrated in Fig. 1d. In the FCC LiF lattice, each Li^+ ion occupies an octahedral site surrounded by six F^- ions (drawn in green in Fig. 1d), while the tetrahedral sites (drawn in yellow in Fig. 1d) remain empty.

We replicated the conventional cell shown in Fig. 1d five times along the three Cartesian axes, resulting in a final simulation box with a volume of approximately 20 × 20 × 20 Å^3. The resulting supercell was simulated at 300 K keeping constant volume, number of atoms, and temperature. Figure 2a and b compare the radial distribution functions (RDFs) between Li and F for the ReaxFF[40] and our MLIP. Both force fields generate peaks consistent with the FCC crystal structure, with an average Li-F interatomic distance of approximately 2 Å. However, after a short equilibration period (~100 ps), the ReaxFF RDF exhibits progressively broader peaks and a notable shift, indicating excessive atomic mobility. This phenomenon is in agreement with previous observations[40–43] that ReaxFF struggles to accurately describe the LiF crystal phase, leading over time to partial amorphization. In contrast, our MLIP preserves the expected FCC structure over nanosecond timescales, confirming its ability to accurately describe the ionic bonding in LiF.

To further assess the MLIP stability, we carried out NVT simulations at five temperatures, ranging from 250 K to 450 K with steps of 50 K (Fig. 2c). This range spans typical LIBs working conditions as well as extreme scenarios approaching thermal runaway[44] (e.g., the Tetramethylene sulfone (TMS) base electrolyte flash point is ~440 K [45]). Across this interval, the Li-F RDFs show systematic peak broadening with temperature, consistent with thermal motion and indicating that the MLIP maintains a stable crystal phase and accurately reproduces lattice vibrations. To further validate the MLIP beyond finite-temperature structural stability, its phonon dispersion and equation of state were compared to the underlying ab initio reference and the ReaxFF (Supplementary Fig. S4). The MLIP closely reproduces both the DFT phonon spectrum and the equilibrium-volume minimum, whereas ReaxFF exhibits pronounced deviations from DFT.

Vacancy diffusion

Confident in the accuracy of the MLIP, we next investigated the Li-ion diffusion in LiF. Several atomistic mechanisms can, in principle, contribute to Li mobility: point-defect migration via vacancies or interstitial sites and pathway enlargement as a consequence of lattice deformation at grain boundaries, and collective motions such as paddlewheel-like motion or ring-diffusion hops involving multiple ions[9]. Because the present study focuses strictly on bulk phenomena, we exclude grain-boundary and surface pathways, which will be studied in the future.

We start by studying the diffusion via Li-vacancy since Handan Yildirim et al.[46] found that these defects are thermodynamically more stable than other point defects like interstitials and Frenkel pairs. Their DFT formation-enthalpy calculations indicate that lithium vacancies disrupt the close-packed nature of the rock-salt structure less significantly, with an energy of approximately 0.76 eV for Li vacancies compared to about 1.73 eV for Li interstitials. More complex point defects, such as Schottky defects and Frenkel defects, have even higher formation energies (>2.3 eV[46]), so we excluded them from our study.

In vacancy-mediated diffusion (a missing Li-ion in the octahedral site), one of the twelve surrounding Li atoms hops into the empty site, allowing the lithium atom motion, as schematically illustrated in Fig. 3a. To model this process, we created a single vacancy by removing one Li atom from the 5 × 5 × 5 LiF supercell used for the bulk simulation, resulting in a well-isolated defect with minimal vacancy-vacancy interactions with the periodic image. Unbiased NVT simulations (30 ns, four replicas, 250−450 K) revealed no vacancy hops, in line with previous ab initio Climbing Image Nudged Elastic Band (CI-NEB) studies that reported a relatively high activation energy for this process (0.66 eV for Zheng et al.[47] and 0.73 eV for Yildirim et al.[46]). At 450 K, such barriers roughly translate into a characteristic diffusion time of the order of microseconds, which explains our inability to observe vacancy diffusion on the 20 ns timescale. To overcome this timescale problem, we used the on-the-fly probability enhanced sampling (OPES) method[48,49], which accelerates rare events sampling by adding a bias potential along a selected collective variable (CV). Because the twelve Li^+ neighboring the vacancy are symmetrically equivalent, the choice of which Li to bias does not affect the reaction pathway or the free energy barrier. Thus, we biased one arbitrarily chosen neighbor of the vacancy, and set as collective variable, $\mathbf{s}$, for the process, the two cartesian coordinates $\mathbf{s} = (x, y)^T$ (any of the three cartesian coordinate pairs is equally valid because of cubic symmetry).

The reconstructed FES is plotted in Fig. 3b, together with the minimum-free-energy reaction pathway ζ and the resulting free energy barrier. From the two-dimensional free-energy surface, we

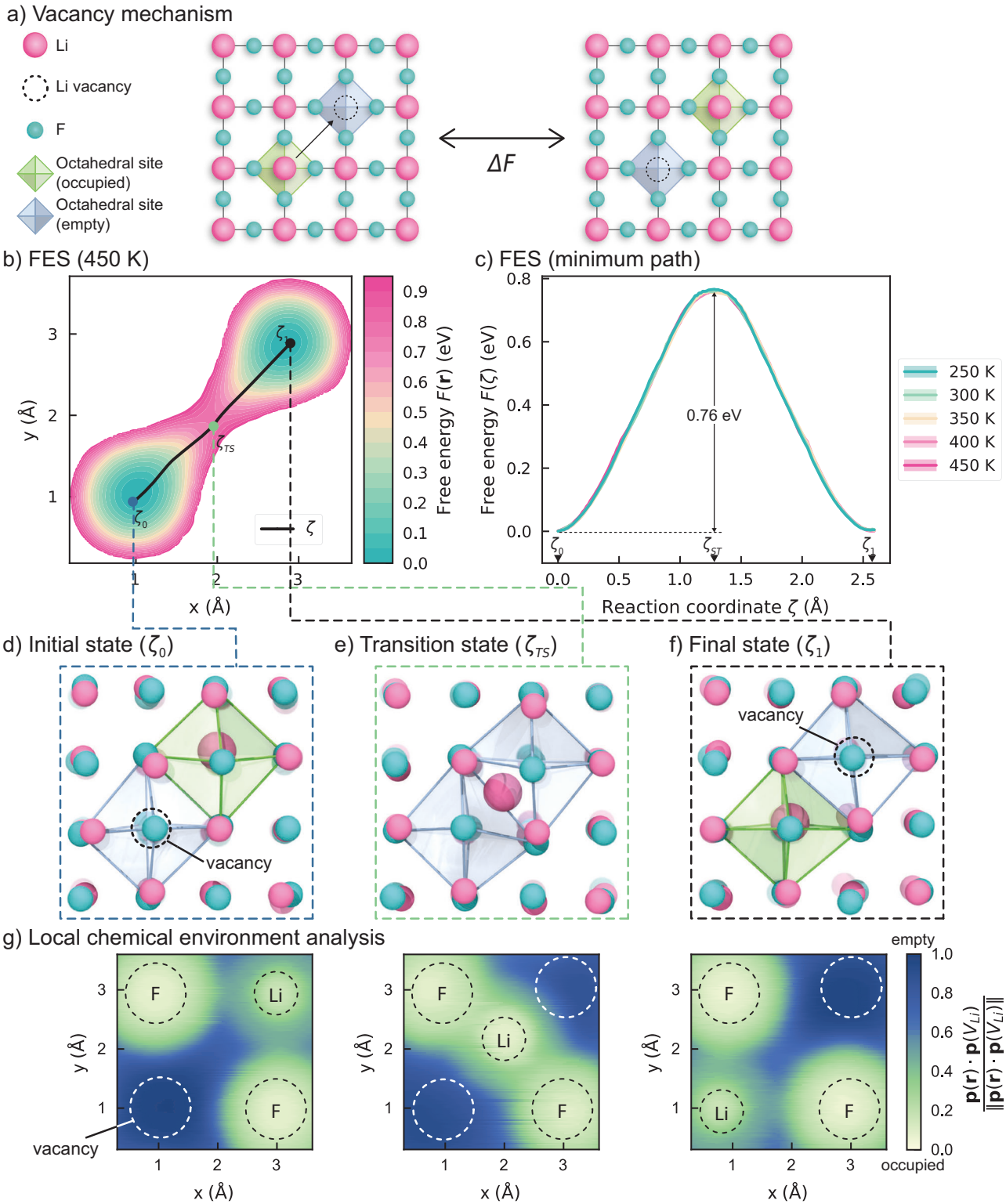


Fig. 3 | Vacancy mechanism. a Simplified schematic representation of a lithium vacancy Li^+ hop. Free energy analysis from metadynamics simulation: in (**b**) the two-dimensional FES in CV space $\mathbf{s} = (x, y)^T$, and in (**c**) the free energy barrier $G = G(\zeta)$ along the reaction coordinate ζ resulted from minimum energy pathway analysis[88]. MD frames for the initial (**d**), transitional (**e**), and final (**f**) states of the reaction. Color code: Li atoms in magenta, the F atoms in green, and the transparent blue atom is the vacancy site. **g** Local chemical environment analysis: cosine similarity between SOAP descriptors at the virtual vacancy position $\mathbf{p}(V_{Li})$ and at a general position $\mathbf{p}(\mathbf{r})$.

extracted vacancy-migration barriers at 250, 300, 350, 400, and 450 K (Fig. 3c), yielding a temperature-independent activation energy of 0.76 eV.

To gain further insight into the vacancy-diffusion mechanism, we performed an analysis of the local chemical environment during the diffusion process (Fig. 3g). Here we use the smooth overlap of atomic positions (SOAP) descriptor[50] at arbitrary points $\mathbf{r}$ in the unit cell by placing a Li "ghost" atom and evaluating the local neighbor density, yielding a feature vector $\mathbf{p}(\mathbf{r})$. This was compared with the SOAP descriptor of ideal vacancy site, $\mathbf{p}(V_{Li})$, using the cosine similarity in Fig. 3g. The similarity map

shows that, when the hopping Li reaches the transition state, only two high-similarity vacancy sites are available, confirming a unique, symmetry-defined hop channel.

Finally, to roughly estimate diffusivity timescale, we used the approximated formula $D = \delta^2/(g\tau)$ where $\delta = \zeta_0 - \zeta_1 = 2.6$ Å is the diffusion step, $g = 6$ accounts for the three equivalent vacancy directions, and τ is the characteristic diffusion time. The value of τ was estimated using the calculated activation energy within the Eyring rate equation: $\tau = \nu^{-1} \exp(E_a/k_B T) = 0.94$ s, where $\nu = k_B T/h = 6.3 \times 10^{12}$ Hz is the thermal attempt frequency (see Supplementary Information, Section 1.3). This yields a diffusivity at 300 K of approximately $D(300\,\mathrm{K}) \approx 1.2 \times 10^{-16}$ cm^2/s, confirming that diffusion via vacancies in LiF is negligible over the battery operational timescale.

Interstitial diffusion

The next diffusion pathway considered is Li interstitial migration. Here, to model this defect, we added a single Li atom into the supercell used for the pure bulk LiF studies and placed it at a tetrahedral metastable site (Fig. 1d). In the absence of a neighboring vacancy (i.e., no Frenkel pair), two mechanistic options are available in the LiF rock-salt lattice: direct hopping and knock-off mechanism. The first mechanism consists of the interstitial Li jumping to the next tetrahedral cage by squeezing between stationary lattice ions, while in the second, the interstitial Li pushes a neighboring octahedral Li into an adjacent empty tetrahedral site, while the initial interstitial atom moves into the empty octahedron, as illustrated in Fig. 4a diagram.

MD simulations were performed in the NVT ensemble at 250 K, 300 K, 350 K, 400 K, and 450 K. Across all trajectories, lithium ions migrated spontaneously and exclusively via the knock-off mechanism, in line with first-principles CI-NEB results in which the knock-off pathway displayed the activation barrier of 0.27 eV[46] and 0.25 eV[47], while direct interstitial hopping required roughly double that energy (0.54 eV[47] and 0.56 eV[46]).

Furthermore, using the Einstein-Smoluchowski relation $\left(D = \frac{1}{6}\frac{\mathrm{d}}{\mathrm{dt}}\langle \Delta \mathbf{r}^2 \rangle\right)$ we computed the Li diffusion coefficient by fitting the slope of the mean-square displacement $\left(\mathrm{MSD} = \langle \Delta \mathbf{r}^2 \rangle\right)$ once it reached a linear regime. Due to the nature of knock-off diffusion, we first calculate the *per-ion* MSD $\left(\langle \Delta \mathbf{r}^2 \rangle / N_{Li}\right)$, average over all the Li in the simulation box. Thus, to obtain the MSD for the diffusivity, we multiply the *per-ion* MSD by the number of Li atoms, following standard practice[51]. The average diffusivity values at different temperatures were then fitted to the Arrhenius equation[52,53]

$$D(T) = D_0 \exp\left(-\frac{E_a}{k_B T}\right), \tag{1}$$

where D_0 is the effective maximum diffusivity at infinite temperature, E_a denotes the activation energy, k_B is the Boltzmann constant, and T is the simulation temperature. D_0 exhibits weak temperature dependence (e.g., $D_0 = g\delta^2 k_B T/h$, see Supplementary Information). These contributions are incorporated into a constant prefactor within the current Arrhenius formulation for the studied temperature range.

The results of this analysis are shown in the Arrhenius plot in Fig. 4b, alongside analogous analyses from ReaxFF and the DFT prediction. The unbiased MD simulation showed an activation energy of $E_a = (0.24 \pm 0.01)$ eV and pre-exponential factor of $D_0 = (3.3 \pm 0.9) \times 10^{-3}$ cm^2/s. In contrast, the ReaxFF trajectory gives $E_a = 0.06$ eV and a large prefactor, which reflects its difficulty in maintaining the LiF crystalline phase, leading to gradual partial amorphization[40,54,55].

The activation energy obtained with the MLIP is also in agreement with the ab initio CI-NEB value (0.27 eV[46], 0.25 eV[47]).

Given the relatively low knock-off barrier, the relevance of non-Arrhenius effects within the investigated temperature range was explicitly verified[56]. By comparing the Arrhenius[52,53] description with an Ornstein-Uhlenbeck model[56] and direct MD-derived crossing times, we found that the deviations are negligible over 250−450 K (see Supplementary Information, Sections S1.3–S1.4).

An initial ideal estimate of the ionic conductivity in bulk LiF is obtained by combining defect formation energies reported by Yildirim et al.[46] with the diffusivities determined in this study. This calculation employs the dilute-limit Nernst-Einstein approximation[57]:

$$\sigma = D\,c\,\frac{q^2 F^2}{RT}, \tag{2}$$

where q denotes the carrier valence charge ($|q| = 1$), F represents the Faraday constant, and R is the ideal gas constant. The equilibrium carrier concentration is approximated by $c = c_{\max} \exp\left(-E_f/k_B T\right)$. Using $E_f(i) = 1.73$ eV for the interstitial defect and a charge-neutral vacancy estimate $E_f(V) \approx E_f(V_{\mathrm{Li}}) + E_f(V_{\mathrm{F}}) = 1.52$ eV[46], and assuming 8 interstitial and 4 vacancy sites per unit cell as max concentration $c_{\max}$, the concentrations at 300 K are calculated as $c_i \approx 1.2 \times 10^{-6}$ cm^{-3} and $c_V \approx 1.9 \times 10^{-3}$ cm^{-3}. The corresponding conductivity contributions are $\sigma_i \approx 1.05 \times 10^{-6}$ S cm^{-1} for interstitial and $\sigma_V \approx 8.81 \times 10^{-13}$ S cm^{-1} for vacancies. Therefore, while interstitials are thermodynamically less favorable, their substantially higher mobility leads to a greater transport contribution than vacancies, making them the dominant charge carrier in bulk LiF.

To gain further mechanistic insight into the transport kinetics, we analyzed individual knock-off events using the following order parameter:

$$s = d_1 - d_2 = \|\mathbf{r}_1 - \mathbf{r}_0\| - \|\mathbf{r}_2 - \mathbf{r}_0\|, \tag{3}$$

where $\mathbf{r}_0$ is the ideal octahedral position, and d_i is the instantaneous distance from that site to Li atoms $\mathbf{r}_1$ (the migrating interstitial) and $\mathbf{r}_2$ (the lattice Li that will be displaced) as illustrated in Fig. 4a inset. With this coordinate, the initial state is identified at $s \approx -1.5$ Å (Fig. 4d), the transition state at $s \approx 0.0$ Å (Fig. 4e), and the final state at $s \approx 1.5$ Å (Fig. 4f). After the first knock-off event has taken place, the identity of the interstitial atom changes because any Li can potentially occupy a tetrahedral site. We, therefore, applied an unsupervised ML classifier that encodes each Li's local environment with a SOAP descriptor[50] combined with density-based clustering to re-identify, at every frame, the two atoms involved in the knock-off diffusion (see Methods). At every trajectory frame, the classifier labels the tetrahedral Li atoms, and by looking at the time evolution of the label, it is possible to track the tetrahedral-octahedral pair, allowing continuous definition of $s(t)$ throughout the 160 ns (40 ns × 4) trajectory for each temperature. This SOAP-based chemical environment descriptor for diffusion ion identification is conceptually related to the descriptor-based analysis framework proposed by Kahle et al.[58]. However, rather than identifying carrier sites, our method focuses on locating atoms that contribute to mass transport.

Analysis of $s(t)$ reveals that knock-off proceeds in two stages. (i) *Approach*: thermal fluctuations shorten d_1 while d_2 increases until s nears zero. (ii) *Engagement*: both Li-ions wiggle together in the octahedral region ($s \approx 0$) until one of them falls into the adjacent tetrahedral site, completing the exchange. The "dwell time" in the engagement zone is quantified as $\Delta t(s = 0)$, namely the time spent within the interval $[-0.25, 0.25]$ Å. Violin plots in Fig. 4c show that the mean dwell time decreases linearly with the temperature from $\langle \Delta t(s=0) \rangle = 0.11$ ps at 250 K to $\langle \Delta t(s=0) \rangle = 0.08$ ps at 450 K, as for the maximum observed dwell time (from $\max[\Delta t(s=0)] = 0.29$ ps at 250 K to $\max[\Delta t(s=0)] = 0.24$ ps at 450 K). This trend indicates that at lower temperatures, the coupled Li pair oscillates longer in the octahedral pocket before completing the diffusion step, whereas the elevated thermal energy forces the system across the saddle, shortening the engagement phase.

Ring diffusion

Leveraging the large system sizes and long time scales accessible with MLIP-based MD, we next examined the dynamics of two Li interstitials. The defects were initialized at the maximum possible separation within the cell to minimize initial interstitial-interstitial interactions.

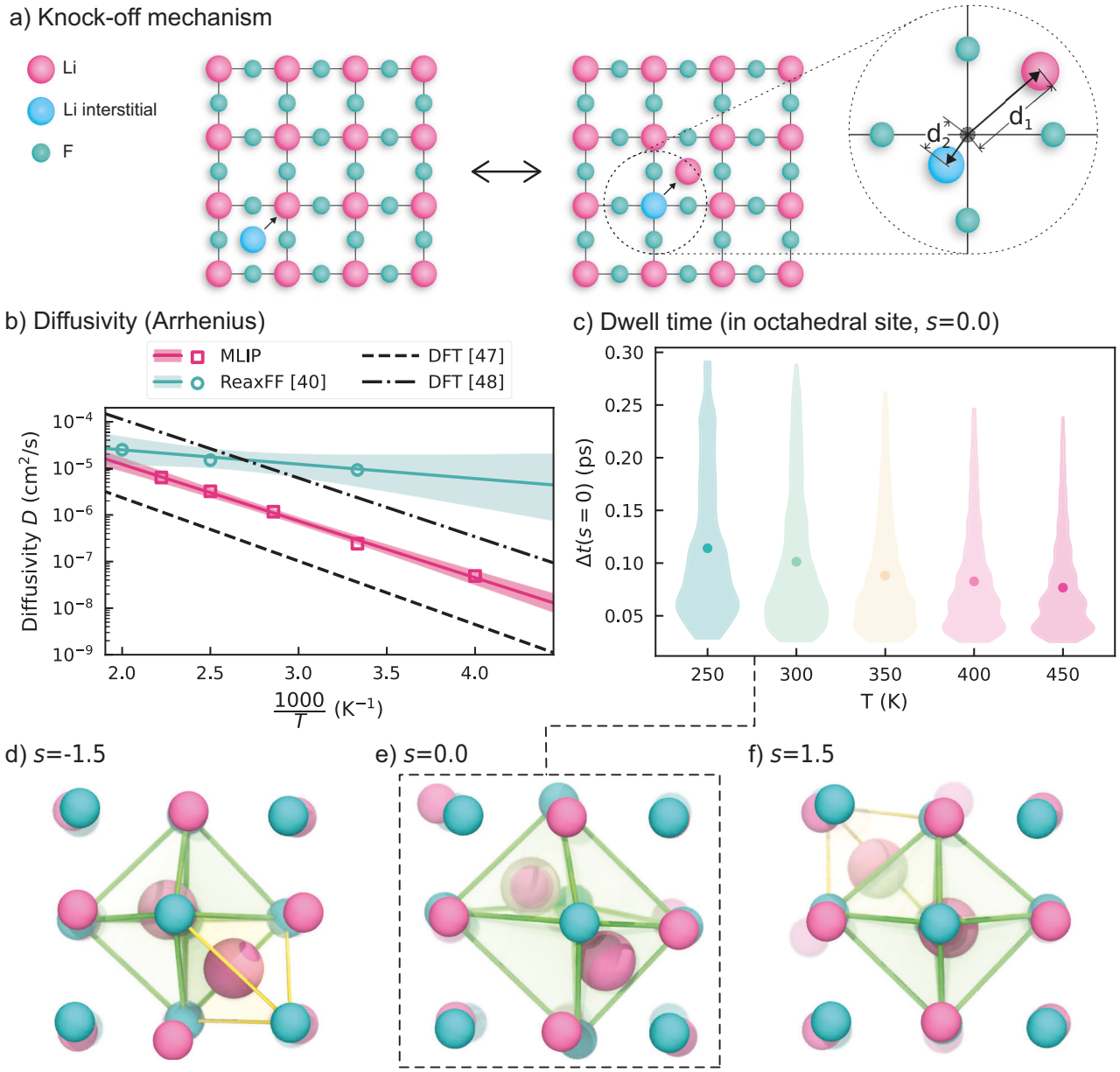


Fig. 4 | Interstitial knock-off mechanism. a Simplified schematic representation of a lithium Li^+ interstitial Knock-off. Kinetic analysis: in (**b**) the Arrhenius plot of the Li self-diffusion coefficient obtained from DFT and transition-state theory by Yildirim et al.[46] (black dashed line) and by Zheng et al.[47] (black dash-point line), with ReaxFF[40] (green circles and line) and with MLIP (magenta squares and line). The square point for the MLIP was obtained by averaging the diffusivity calculated from 4 replicas, each 40 ns long. Shaded bands represent the interpolation 95 % confidence interval. **c** Violin plots of the dwell time, $\Delta t(s = 0)$, spent in the octahedral region; solid dots denote the mean dwell time at each temperature. MD frames for the initial (**d**), transitional (**e**), and final (**f**) states of the reaction. Color code: Li atoms in magenta, the F atoms in green.

As above, 5 unbiased NVT at 250 K, 300 K, 350 K, 400 K, and 450 K were carried out for a minimum simulation length of 20 ns, with longer times for low temperature runs.

Initially, each interstitial Li atom performed isolated knock-off jumps. However, after several hops, the two defects can be found in two neighboring cells, and a new diffusion mechanism emerges: we observe the formation of collective motion involving six Li-ions instead of the four (two for each interstitial atom added) atoms during the knock-off. As illustrated in Fig. 5a, when the two atoms approach each other, they begin to engage with Li in the nearby octahedral site. This interaction leads to an unexpected further engagement with the other two Li atoms in the octahedral arrangement, forming a ring-like structure (Fig. 5b). Similar formations were observed in cubic Li salts or Li alloys, as seen in related systems such as by Kirsch et al.[59] and Moon et al.[60] for $Li_{12}Si_7$, and Kvist et al.[61] for Li_2SO_4.

To rule out finite-size artifacts, we repeated the two-interstitial simulations in larger supercells: an $8 \times 8 \times 8$ ($31.2 \times 31.2 \times 31.2$ Å^3), a $10 \times 10 \times 10$ ($39 \times 39 \times 39$ Å^3), a $12 \times 12 \times 12$ ($46.8 \times 46.8 \times 46.8$ Å^3), and a $15 \times 15 \times 15$ ($58.5 \times 58.5 \times 58.5$ Å^3), containing 4098, 8002, 13,826, and 27,002 atoms, respectively. In each case, the two interstitial Li were placed at the maximally separated tetrahedral sites, and unbiased MLIP MD simulations were run at 450 K to accelerate diffusion. In all supercells, the six-ion ring exchange re-emerged following a progressively longer transient period δt_0. This observation aligns with a ring-formation time that scales inversely with the interstitial concentration $\delta t_0\, c = 87.5$ ps mol L^{-1} (see Supplementary Information, Section S2.5). Once the defects diffused into neighboring cells, six-Li ring motion occurred, consistent with observations in the $5 \times 5 \times 5$ cell. This size-independent behavior suggests that the ring mechanism is intrinsic to LiF at elevated local interstitial concentration and is not an

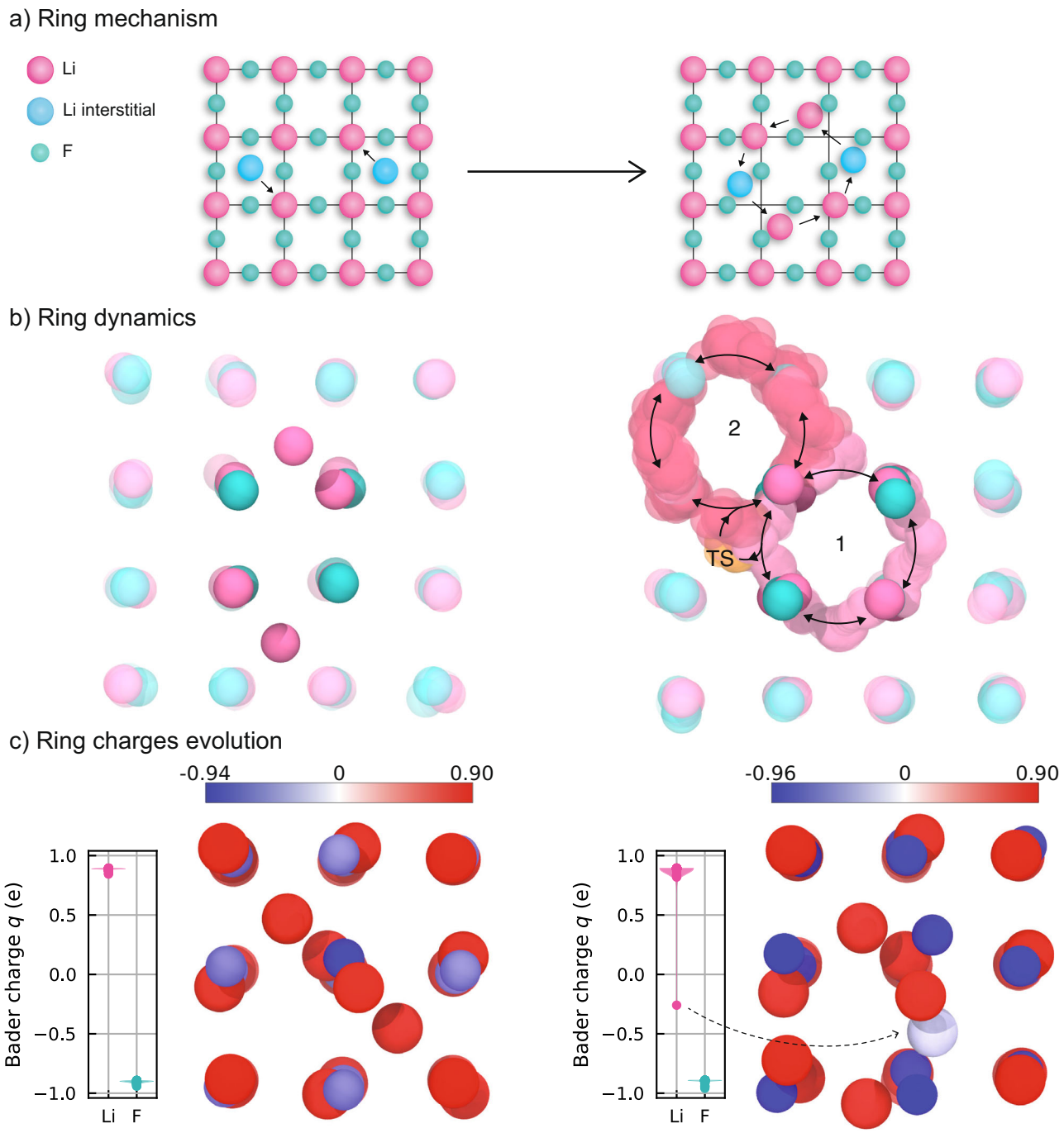


Fig. 5 | Interstitial ring mechanism. a Schematic of a six ion ring formed by the initial two Li^+ interstitials. **b** Ring dynamics. The left panel shows a snapshot taken just before the two interstitials approach and compete for the octahedral Li atoms. The right panel presents a time overlay of consecutive MD frames, illustrating the formation, breakup, and re-formation of the six-ion ring during a single diffusion step. **c** Bader charge analysis. The left panel shows the charge distribution before ring formation, and the right panel shows the distribution when the ring is fully established. In both panels, the top color maps indicate atomic charges, while the side violin plots summarize the charge distributions for Li and F. For **a** and **b**, Li atoms are shown in magenta and F atoms in green. In (**c**), more positive Bader charge values are shown in red and more negative values in blue; Li and F atoms are additionally distinguished by particle size. In the right panel, Li atoms with reduced Bader charge during ring formation are rendered nearly white.

artifact of periodic boundary conditions or artificially high defect-defect interactions.

We further tested the MLIP against DFT. An MLIP MD snapshot just prior to ring formation in the 3 × 3 × 3 supercell run (left panel in Fig. 5c) was relaxed with the PBE-DFT level of theory (same as the MLIP training set). The DFT relaxation converged to the same six Li ring geometry (right panel in Fig. 5c). DFT thus corroborates that the ring geometry is a genuine local minimum and that the ML potential correctly reproduces this stability.

The DFT snapshot was further analyzed via Bader charge[62], where the valence-electron density, $n(\mathbf{r})$, is integrated over each atom's Voronoi polyhedron. Figure 5c compares the charge distribution immediately before ring formation with that in the fully developed six Li complex. In the starting configuration (left panel of Fig. 5c) Li atoms carry a charge of ≈ 0.90 e while

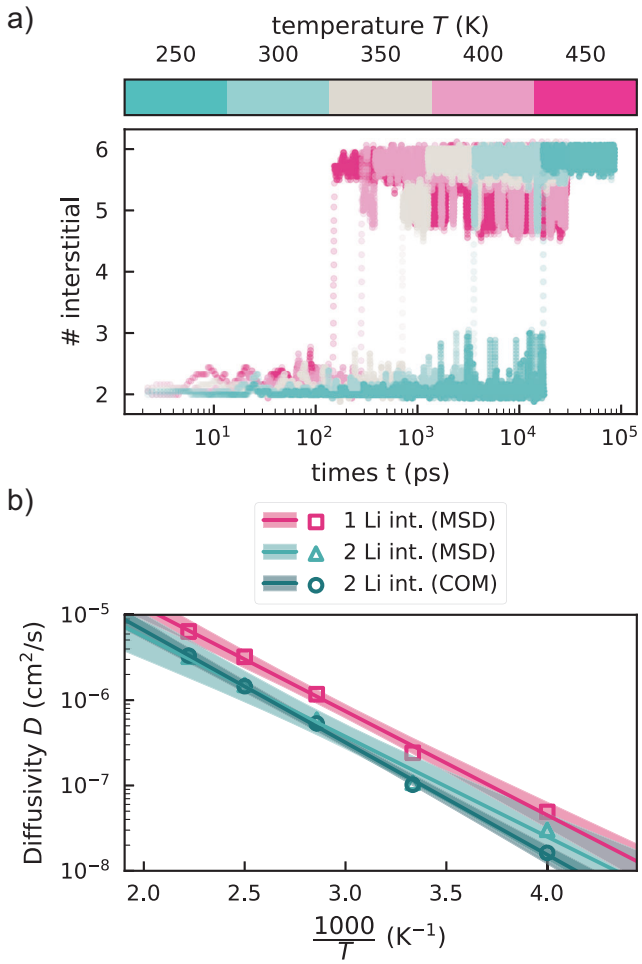


Fig. 6 | Ring mechanisms kinetics. a Time evolution of the number of Li atoms classified as "non-octahedral" by the unsupervised clustering method for the five temperatures (250−450 K). The count is two while the interstitials migrate independently and rise to six once the ring is fully established. **b** Diffusivity comparison. Magenta line and square markers: knock-off pathway (baseline). Light-green line and triangle markers: *raw* tracer-like ring MSD (without the COM correction) from individual ring ions, which includes both collective translation and internal correlated motion of the six-ion structure. Dark-green line and circles markers: collective ring diffusivity after COM correction, which removes internal six-ion fluctuations while retaining net translational motion, thereby representing the true contribution of ring hops to bulk Li transport. Error bands show 95 % confidence limits on the linear Arrhenius fit.

fluoride ions carry $\approx -0.94\,e$, consistent with the largely ionic bonding in LiF.

Upon ring formation, we find that one of the two interstitial Li atoms exhibits a significant reduction in its net positive charge, suggesting a partial valence charge localization (Supplementary Fig. S10) of electronic density around the defect site as visible in the right panel of Fig. 5c. Indeed, this compensating electron density is delocalized over the surrounding fluorine atoms, preserving overall electroneutrality. This partial redistribution of valence charge leads to a reduction in the positive Bader charge associated with the interstitial Li, thereby lowering Coulomb repulsion between neighboring interstitial Li and stabilizing the six-ion arrangement.

Because ring diffusion is a collective event involving six Li ions, it is not adequately characterized by the Einstein-Smoluchowski relation, which relies on tracer-like mean squared displacement (MSD) derived from individual lithium displacements. In this context, the participating ions experience significant correlated internal rearrangements alongside any net displacement of the ring object[63,64]. Indeed, Van der Ven et al.[63] and Marcolongo and Marzari[64] emphasize that correlated ionic transport requires distinguishing between single-particle (tracer-like) diffusion and collective transport measures, as the latter depend on correlated displacements among carriers. In the present case, direct application of these formalisms is complicated because the ring mechanism does not involve a fixed number of independently diffusing ions. Instead, it consists of a dynamic six-ion collective rearrangement where individual Li ion displacements are dominated by correlated internal motion alongside the net translation of the ring structure. Therefore, a protocol is proposed that first isolates the six-lithium-ion ring complex and then directly measures the complex's translation. To isolate the kinetics of the collective motion, we first identified, frame by frame, which Li ions participated in the ring, following a procedure similar to the one used in the knock-off study. Then, every Li environment was encoded at each frame using a SOAP descriptor. An unsupervised density-based algorithm then clustered the descriptors into two categories: (i) "octahedral" Li with six F neighbors and (ii) "non-octahedral" Li containing interstitial and ring participants. Figure 6a plots the number of non-octahedral Li detected as a function of time. During the initial phase, when the two defects migrate via knock-off, exactly two Li are classified as non-octahedral; thermal fluctuations increase the noise in this count at higher temperatures. Approaching the ring-formation event, the count suddenly increases and stabilizes at six, indicating the full establishment of the ring configuration. Once the ring is formed, the diffusion continues as a collective motion of the six Li, even if the identity of the atoms involved changes with time. The time required for the onset of this new diffusion regime is inversely proportional to the simulation temperature Fig. 6a.

At each time, we identified the six Li ions involved in the ring, and we treated their center of mass (COM) as a virtual atom, tracking its displacement with respect to its position at the previous step. To reduce possible isolated false positives from the SOAP-based classifier, the ring assignment was checked for consistency also against the preceding and following frames. When the identity of one or more Li ions in the ring changes, this occurs locally within the same compact six-ion complex, so the corresponding COM trajectory remains continuous and does not exhibit artificial numerical jumps in the MSD. Tracking this COM satisfies the single-particle assumption for the Einstein-Smoluchowski relation[63,64] while still capturing the net displacement generated by the collective hop. To compensate for the reduced statistical sampling that comes from following one virtual particle, we performed 12 independent replicas at each temperature, each of them featuring ring formation after some time. The measurement of the MSD started with the formation of the ring. It was averaged over all replicas and then rescaled by the standard three-dimensional normalization from the Einstein relation (1/6). In this way, the resulting diffusion coefficient represents the contribution of ring diffusion to bulk Li transport rather than the mobility of the ring entity itself. From the resulting MSD, we compute the diffusivity at each temperature and, by interpolating the Arrhenius exponential law of Eq. (1), we obtain the diffusivity result in Fig. 6b. The activation energy is $E_a = (0.26 \pm 0.01)$ eV, higher than the knock-off mechanism, while the pre-exponential factor is slightly lower $D_0 = (2.8 \pm 0.6) \times 10^{-3}$ cm^2/s. Consequently, at all temperatures studied, the ring pathway is slightly less efficient than knock-off diffusion, despite the extra degrees of freedom provided by the second interstitial. This finding indicates that, in LiF, increasing Li concentration beyond the single-interstitial regime does not necessarily accelerate ion transport; instead, strong Li-Li interactions impose an energetic penalty that offsets the geometric advantage of a collective hop.

Discussion

In conclusion, we used molecular dynamics simulations based on machine learning-based interatomic potentials to study lithium diffusion in bulk LiF, a critical inorganic component of the solid electrolyte interphase in lithium-ion batteries. Previous approaches based on classical or reactive force fields have proven inadequate due to their inability to reproduce the correct lattice dynamics, while ab initio methods, due to their computational cost, cannot access such long timescales. The use of MLIPs, thus, bridges this long-

standing gap, delivering both quantum-level accuracy and sufficient computational efficiency to observe these diffusion phenomena.

Furthermore, our simulations successfully captured vacancy and interstitial diffusion processes and revealed a collective ring diffusion mechanism involving six lithium atoms, which is enabled by high interstitial concentrations and stabilized by partial charge delocalization. We further propose a SOAP-based local-environment analysis coupled with unsupervised clustering and ML classifiers to enable quantitative analysis of diffusion kinetics. Remarkably, the MLIP predicted the charge rearrangement and the emergence of the six-ion ring even before the introduction of training examples of such collective motion, showing the extrapolation and exploration power of these potentials. This kind of unexpected observation and many-body pathway is inaccessible to classic and ReaxFF force fields due to their fixed analytic functional forms, which constrain the potential-energy surface and limit the representation of collective motion and charge transfer, while we show that the data-driven MLIP naturally learns it. Given that the SEI undergoes continuous restructuring and lithium accumulation during battery operation, especially under cycling and overcharge conditions, we hypothesize that such ring-like diffusion events could become transiently accessible in LiF-rich SEI domains.

The mechanistic conclusions reported here — namely the intrinsic vacancy/interstitial hierarchy and the existence of a collective six-ion ring pathway — are properties of bulk-like crystalline LiF and therefore serve as physically grounded reference limits for LiF-rich SEI domains. However, quantitative transport rates and dominant carriers in real SEIs will depend on microstructure, including grain boundaries, phase interfaces, and disorder, which may introduce faster percolating pathways. Thus, bulk-LiF diffusion should be interpreted as a bounding case rather than assumed rate control in heterogeneous SEI environments.

Overall, this work represents an initial but crucial step towards the comprehensive modeling of the SEI. The iterative active learning protocol can be extended to systematically incorporate chemical heterogeneity, interfacial phenomena, and dynamic structural disorder in future multiscale simulations. The machine learning method developed in this work will enable close tracking of lithium transport in grain boundaries, interfaces, and disordered systems to further investigate mechanisms within the SEI reactive environment.

Methods

The following section provides a detailed description of the computational methods employed in this work, from the MLIP training and testing to the ML-based classification method for defect identification (additional technical details are available in the supplementary file).

MLIP training

The MLIP was trained following an active learning protocol, as e.g., in M. Yang et al.[65,66]. We began with an initial set of configurations for all systems studied (bulk LiF, LiF with a vacancy, and LiF with an interstitial) extracted from a ≈ 50 ps ab initio molecular-dynamics (AIMD) trajectory of a $3 \times 3 \times 3$ supercell in the NVT ensemble at $300 - 700$ K, chosen to accelerate phase-space exploration and sampled every 0.1 ps. AIMD runs were carried out with CP2K[67] using the Perdew-Burke-Ernzerhof (PBE) exchange-correlation functional[68]. The $3 \times 3 \times 3$ LiF supercell balances computational efficiency and accuracy.

At this stage, CP2K was used only to generate physically meaningful candidate geometries for the initial data pool; the energies and forces used as reference labels for MLIP training were not taken from CP2K. Because these trajectories served only to collect geometries for the training set, we employed less demanding computational settings: a single-zeta Gaussian basis (SZV-MOLOPT) for valence electrons, Goedecker-Teter-Hutter (GTH) PBE optimized pseudopotentials[69] for core electrons with a plane-wave cutoff of 280 Ry. Brillouin-zone sampling was restricted to the Γ-point of the supercell.

The training then proceeded through iterated "active-learning" cycles, during which an error proxy was evaluated every 0.01 ps along the MLIP-MD trajectories by measuring the deviation in predicted forces among a committee of 4 MLIP models trained on the same dataset. Specifically, configurations exhibiting force deviations greater than 50 meV Å^{-1} and less than 350 meV Å^{-1} were randomly selected as candidates for relabeling, as these represent the most informative data points while excluding well-learned structures and strongly nonphysical outliers. The final data set contains ≈ 59, 100 structures (≈46, 300 training, ≈12, 800 validation).

Reference energies and forces for both the initial pool and the subsequent active-learning additions were computed with DFT using the Quantum ESPRESSO (QE) code[70–72]. Projector-augmented-wave (PAW) pseudopotentials (PP) for Li and F, compatible with the PBE exchange-correlation functional[68] and a scalar relativistic flavor, taken from the QE PP library. Brillouin-zone sampling was limited to the Γ-point. Kohn-Sham wavefunctions were expanded in a plane-wave basis with kinetic-energy and charge-density cutoffs of 110 Ry and 440 Ry, respectively. Electronic occupations were treated with Gaussian smearing, with 0.005 Ry as a spreading value for Brillouin-zone integration. The convergence threshold for self-consistent field (SCF) was fixed to 5×10^{-7} Ry, using local Thomas-Fermi charge mixing (TF-local) strategy[73], and mixing parameter $\beta = 0.2$. All defective configurations considered in this work (vacancy, single interstitial, and two interstitials) were treated as neutral non-stoichiometric periodic supercells, with the total charge set to zero in the QE calculations.

The Li-F MLIP was trained with DeepMD-kit v2 package[74–76]. The MLIP architecture consists of Deep Potential-Smooth Edition (DeepPot-SE) descriptors[77] with an embedding neural network (NN), consisting of three fully connected layers with 30, 60, and 120 neurons, respectively, to encode the chemical local environment, and a four-layer residual NN (ResNN)[78] with 240 neurons per layer as the fitting NN. For the neighboring atoms used for the descriptors, we chose a 6 Å cutoff. We used the Adam optimiser[79] with an initial learning rate of 1×10^{-3}; the rate decayed by a factor of 0.94 every 5000 steps. A total of 1×10^{9} training steps were executed with a batch size of 4. The final model reaches DFT-like accuracy, showing a validation-set root mean square error (RMSE) of 1.6 meV atom^{-1} for energies and 42.7 meV Å^{-1} for force components (Supplementary Fig. S3).

MLIP molecular dynamics

All MLIP molecular dynamics simulations were carried out with the open-source code LAMMPS[80]. Both unbiased and biased trajectories were integrated with the velocity-Verlet algorithm using a 0.25 fs timestep under periodic boundary conditions. Each run was preceded by a 250 ps equilibration phase. NVT ensemble was used for both equilibration and production trajectories, with the velocity-rescaling thermostat[81] and relaxation time $\tau = 0.02$ ps. During active-learning, the training dataset was built using a $3 \times 3 \times 3$ LiF supercell to reduce SCF cost for DFT labeling. Unless stated otherwise, production simulations employed a $5 \times 5 \times 5$ conventional LiF supercell (1000 atoms) for the bulk configuration. The simulation volume was determined from the equilibrium bulk LiF structure relaxed at the QE level of theory, and this cell was then kept fixed during the NVT simulations. Four independent replicas for every temperature and defect type were employed to gain statistical robustness; for the ring mechanism, we used 12 replicas to suppress noise in the MSD.

Enhanced sampling MD (OPES)

The timescale limitations of vacancy diffusion were overcome with the On-the-fly Probability Enhanced Sampling (OPES)[48,49] method using the PLUMED[82,83] plug-in for LAMMPS. For our *biased* simulation, we set the OPES barrier (ΔE = 0.9 eV), slightly above the NEB-estimated migration barrier (~0.7 eV−0.8 eV)[46,47], to ensure barrier crossing while limiting exploration of high free-energy regions[48,49]. The kernel deposition was performed every 0.25 ps. The time evolution of the collective variable, as well as the convergence of the FES obtained using OPES, are provided in the Supplementary Materials (Supplementary Figs. S6, S7 and S8)

ML interstitial identification

To identify "non-octahedral" Li atoms automatically, we implemented a two-stage ML procedure. First, each atomic environment was encoded with

the SOAP descriptor[50,84]. We used three radial Gaussian basis functions with a cutoff of 6 Å, spherical harmonics up to $l_{max} = 2$, and an atomic density smearing width $\sigma = 0.3$ Å. From all trajectories containing interstitials, we randomly selected 1200 frames, encoding 6×10^5 Li atoms. These datasets were clustered with the unsupervised DBSCAN algorithm from scikit-learn[85] library using density parameters $\varepsilon = 9 \times 10^{-3}$ and minimum samples size $n_{\min} = 5$ (Supplementary Fig. S2.a). Because DBSCAN[86] treats isolated points as noise and thus is unsuitable for frame-by-frame labeling, we used the resulting cluster labels to train a histogram-based gradient-boosting classifier (HGBC)[87]. The binary model (octahedral vs non-octahedral) achieved a validation true positive rate of 99% (Supplementary Fig. S2c) and was applied to every trajectory snapshot.

For the ring mechanism (Ring diffusion Subsection) the classifier allowed us to select the six interstitial Li ions and compute their COM for MSD analysis. For the knock-off mechanism (Interstitial diffusion Subsection), the time-dependent label sequence identified the two exchanging Li atoms and the corresponding octahedral site used for the CV and dwell time analysis.

Supplementary information

Complementary to the results discussed in the main manuscript, the Supporting Information collects additional methodological details and validation analyses, covering the active-learning protocol, OPES setup, diffusivity analysis, SOAP-based defect classification, MLIP validation, finite-size and timestep sensitivity checks, vacancy FES convergence, and further electronic-structure and ring-formation investigations.

Data availability

All training and test DFT data, together with the final trained MLIP model, and the training scripts, are publicly available in the Zenodo archive at https://doi.org/10.5281/zenodo.20150453.

Code availability

DFT calculations used for training-set labeling and charge analysis were performed with *Quantum ESPRESSO*[70–72]; ab initio MD was carried out in *CP2K*[67]. Bader charges were computed with the *BADER* code by Prof. Henkelman's Group[62]. All molecular dynamics (MD) simulations in this study were performed using the open-source *LAMMPS* software package[80], with the addition of *PLUMED* plug-in[82] for the enhanced-sampling MD simulations. The MLIPs were built, trained, and tested with the *DeepMD Kit* library[74,75]. All simulation inputs, MLIP settings, active-learning scripts, preprocessing, post-processing, and analysis notebooks used in this work are publicly available at https://github.com/paolodeangelis/lif-defect-and-ring-diffusion.

Received: 22 September 2025; Accepted: 3 May 2026;
Published online: 20 May 2026

References

1. Yoshio, M., Brodd, R. J. & Kozawa, A. (eds) *Lithium-Ion Batteries: Science and Technologies* https://link.springer.com/10.1007/978-0-387-34445-4 Springer New York, New York, NY. (2009)
2. Zeng, X. et al. Commercialization of lithium battery technologies for electric vehicles. *Adv. Energy Mater.* **9**, 1900161 (2019).
3. Balakrishnan, N. T. M. et al. in *The Great History of Lithium-Ion Batteries and an Overview on Energy Storage Devices* (eds Balakrishnan, N. T. M. & Prasanth, R.) *Electrospinning for Advanced Energy Storage Applications* 1–21 http://link.springer.com/10.1007/978-981-15-8844-0_1 Springer Singapore, Singapore. (2021)
4. Amici, J. et al. A roadmap for transforming research to invent the batteries of the future designed within the European Large Scale Research Initiative BATTERY 2030+. *Adv. Energy Mater.* **12**, 2102785 (2022).
5. Masias, A., Marcicki, J. & Paxton, W. A. Opportunities and challenges of lithium ion batteries in automotive applications. *ACS Energy Lett.* **6**, 621–630 (2021).
6. Maisel, F., Neef, C., Marscheider-Weidemann, F. & Nissen, N. F. A forecast on future raw material demand and recycling potential of lithium-ion batteries in electric vehicles. *Resour., Conserv. Recycl.* **192**, 106920 (2023).
7. Bouguern, M. D., M R, A. K. & Zaghib, K. The critical role of interfaces in advanced Li-ion battery technology: A comprehensive review. *J. Power Sources* **623**, 235457 (2024).
8. Goodenough, J. B. & Kim, Y. Challenges for rechargeable Li batteries. *Chem. Mater.* **22**, 587–603 (2010).
9. Jun, K., Chen, Y., Wei, G., Yang, X. & Ceder, G. Diffusion mechanisms of fast lithium-ion conductors. *Nat. Rev. Mater.* **9**, 887–905 (2024).
10. Vorauer, T. et al. Impact of solid-electrolyte interphase reformation on capacity loss in silicon-based lithium-ion batteries. *Commun. Mater.* **4**, 1–12 (2023).
11. He, Y. et al. Progressive growth of the solid-electrolyte interphase towards the Si anode interior causes capacity fading. *Nat. Nanotechnol.* **16**, 1113–1120 (2021).
12. Li, J., Hu, X. & Li, T. Simulation of Solid Electrolyte Interphase Growth for Lithium Batteries Based on kinetic monte Carlo. *Energy Mater. Adv.* **5**, 0137 (2024).
13. Jagger, B. & Pasta, M. Solid electrolyte interphases in lithium metal batteries. *Joule* **7**, 2228–2244 (2023).
14. Li, Y. et al. Atomic structure of sensitive battery materials and interfaces revealed by cryo-electron microscopy. *Science* **358**, 506–510 (2017).
15. Wi, T.-U. et al. Revealing the dual-layered solid electrolyte interphase on lithium metal anodes via cryogenic electron microscopy. *ACS Energy Lett.* **8**, 2193–2200 (2023).
16. Zhang, Y. et al. Synergetic regulation of SEI mechanics and crystallographic orientation for stable lithium metal pouch cells. *Nat. Commun.* **15**, 4454 (2024).
17. Peled, E., Golodnitsky, D. & Ardel, G. Advanced model for solid electrolyte interphase electrodes in liquid and polymer electrolytes. *J. Electrochem. Soc.* **144**, L208–L210 (1997).
18. Cheng, X. et al. A review of solid electrolyte interphases on lithium metal anode. *Adv. Sci.* **3**, 1500213 (2016).
19. Aurbach, D. et al. New insights into the interactions between electrode materials and electrolyte solutions for advanced nonaqueous batteries. *J. Power Sources* **81-82**, 95–111 (1999).
20. Christensen, J. & Newman, J. A mathematical model for the lithium-ion negative electrode solid electrolyte interphase. *J. Electrochem. Soc.* **151**, A1977 (2004).
21. Wu, B. et al. Li-growth and SEI engineering for anode-free Li-metal rechargeable batteries: A review of current advances. *Energy Storage Mater.* **57**, 508–539 (2023).
22. Tan, J., Matz, J., Dong, P., Shen, J. & Ye, M. A growing appreciation for the role of LiF in the solid electrolyte interphase. *Adv. Energy Mater.* **11**, 2100046 (2021).
23. Wang, Y. et al. Fluorination in advanced battery design. *Nat. Rev. Mater.* **9**, 119–133 (2023).
24. Fan, X. et al. Fluorinated solid electrolyte interphase enables highly reversible solid-state Li metal battery. *Sci. Adv.* **4**, eaau9245 (2018).
25. Jankowski, P., Wieczorek, W. & Johansson, P. SEI-forming electrolyte additives for lithium-ion batteries: development and benchmarking of computational approaches. *J. Mol. Model.* **23**, 6 (2017).
26. Fan, X. et al. Highly fluorinated interphases enable high-voltage Li-metal batteries. *Chem* **4**, 174–185 (2018).
27. Tian, Z. et al. Electrolyte solvation structure design for sodium ion batteries. *Adv. Sci.* **9**, 2201207 (2022).
28. Vanleeuw, D., Sapundjiev, D., Sibbens, G., Oberstedt, S. & Salvador Castiñeira, P. Physical vapour deposition of metallic lithium. *J. Radioanal. Nucl. Chem.* **299**, 1113–1120 (2014).
29. Xie, J. et al. Stitching h-BN by atomic layer deposition of LiF as a stable interface for lithium metal anode. *Sci. Adv.* **3**, eaao3170 (2017).

30. Fan, L., Zhuang, H. L., Gao, L., Lu, Y. & Archer, L. A. Regulating Li deposition at artificial solid electrolyte interphases. *J. Mater. Chem. A* **5**, 3483–3492 (2017).
31. Zhang, X. et al. Columnar lithium metal anodes. *Angew. Chem. Int. Ed.* **56**, 14207–14211 (2017).
32. Chang, W., Park, J. H. & Steingart, D. A. Poor man's atomic layer deposition of LiF for additive-free growth of lithium columns. *Nano Lett.* **18**, 7066–7074 (2018).
33. Chen, L. et al. Novel ALD chemistry enabled low-temperature synthesis of lithium fluoride coatings for durable lithium anodes. *ACS Appl. Mater. Interfaces* **10**, 26972–26981 (2018).
34. Liu, X. et al. Probing the heterogeneous nature of LiF in solid-electrolyte interphases. *Nature* https://www.nature.com/articles/s41586-025-09498-7 (2025).
35. Zhang, S. et al. Tackling realistic Li+ flux for high-energy lithium metal batteries. *Nat. Commun.* **13**, 5431 (2022).
36. Qu, H., Zhang, X. & Su, B.-L. The real face of LiF. *Natl. Sci. Rev.* **12**, nwaf448 (2025).
37. CRC Handbook of Chemistry and Physics, 86th Edition Edited by David R. Lide (National Institute of Standards and Technology). CRC Press (an imprint of Taylor and Francis Group): Boca Raton, FL. 2005. 2544 pp. $125.96. ISBN 0-8493-0486-5. *J. Am. Chem. Soc.* **128**, 5585–5585 (2006).
38. Yun, K.-S. et al. Simulation protocol for prediction of a solid-electrolyte interphase on the silicon-based anodes of a lithium-ion battery: ReaxFF reactive force field. *J. Phys. Chem. Lett.* **8**, 2812–2818 (2017).
39. Wang, Y., Liu, Y., Tu, Y. & Wang, Q. Reductive decomposition of solvents and additives toward solid-electrolyte interphase formation in lithium-ion battery. *J. Phys. Chem. C.* **124**, 9099–9108 (2020).
40. De Angelis, P., Cappabianca, R., Fasano, M., Asinari, P. & Chiavazzo, E. Enhancing ReaxFF for molecular dynamics simulations of lithium-ion batteries: an interactive reparameterization protocol. *Sci. Rep.* **14**, 978 (2024).
41. Han, Y. et al. Development, applications and challenges of ReaxFF reactive force field in molecular simulations. *Front. Chem. Sci. Eng.* **10**, 16–38 (2016).
42. Furman, D. & Wales, D. J. Transforming the accuracy and numerical stability of ReaxFF reactive force fields. *J. Phys. Chem. Lett.* **10**, 7215–7223 (2019).
43. Nagar, A. et al. Reactive Force Field (ReaxFF) and universal force field molecular dynamic simulation of solid electrolyte interphase components in lithium-ion batteries. *J. Electrochem. Energy Convers. Storage* **21**, 021006 (2024).
44. Cappabianca, R., De Angelis, P., Fasano, M., Chiavazzo, E. & Asinari, P. An overview on transport phenomena within solid electrolyte interphase and their impact on the performance and durability of lithium-ion batteries. *Energies* **16**, 5003 (2023).
45. Hess, S., Wohlfahrt-Mehrens, M. & Wachtler, M. Flammability of Li-ion battery electrolytes: flash point and self-extinguishing time measurements. *J. Electrochem. Soc.* **162**, A3084–A3097 (2015).
46. Yildirim, H., Kinaci, A., Chan, M. K. Y. & Greeley, J. P. First-principles analysis of defect thermodynamics and ion transport in inorganic SEI compounds: LiF and NaF. *ACS Appl. Mater. Interfaces* **7**, 18985–18996 (2015).
47. Zheng, J. et al. Lithium ion diffusion mechanism on the inorganic components of the solid-electrolyte interphase. *J. Mater. Chem. A* **9**, 10251–10259 (2021).
48. Invernizzi, M. & Parrinello, M. Rethinking metadynamics: from bias potentials to probability distributions. *J. Phys. Chem. Lett.* **11**, 2731–2736 (2020).
49. Invernizzi, M. & Parrinello, M. Exploration vs convergence speed in adaptive-bias enhanced sampling. *J. Chem. Theory Comput.* **18**, 3988–3996 (2022).
50. De, S., Bartók, A. P., Csányi, G. & Ceriotti, M. Comparing molecules and solids across structural and alchemical space. *Phys. Chem. Chem. Phys.* **18**, 13754–13769 (2016).
51. He, X., Zhu, Y., Epstein, A. & Mo, Y. Statistical variances of diffusional properties from ab initio molecular dynamics simulations. *npj Comput. Mater.* **4**, 18 (2018).
52. Arrhenius, S. Über die Reaktionsgeschwindigkeit bei der Inversion von Rohrzucker durch Säuren. *Zeitschrift für Physikalische Chemie* **4** https://www.degruyter.com/view/j/zpch.1889.4.issue-1/zpch-1889-0116/zpch-1889-0116.xml (1889).
53. Kramers, H. Brownian motion in a field of force and the diffusion model of chemical reactions. *Physica* **7**, 284–304 (1940).
54. Thijs, L. C. et al. Effect of Fe-O ReaxFF on liquid iron oxide properties derived from reactive molecular dynamics. *J. Phys. Chem. A* **127**, 10339–10355 (2023).
55. Gittus, O. R. & Bresme, F. Thermophysical properties of water using reactive force fields. *J. Chem. Phys.* **155**, 114501 (2021).
56. Abkenar, M., Gray, T. H. & Zaccone, A. Dissociation rates from single-molecule pulling experiments under large thermal fluctuations or large applied force. *Phys. Rev. E* **95**, 042413 (2017).
57. Birks, N., Meier, G. H. & Pettit, F. S. *Introduction to the High Temperature Oxidation of Metals* 2 edn https://www.cambridge.org/core/product/identifier/9781139163903/type/book (Cambridge University Press, 2006).
58. Kahle, L., Musaelian, A., Marzari, N. & Kozinsky, B. Unsupervised landmark analysis for jump detection in molecular dynamics simulations. *Phys. Rev. Mater.* **3**, 055404 (2019).
59. Kirsch, C., Dreßler, C. & Sebastiani, D. Atomistic diffusion pathways of lithium ions in crystalline lithium silicides from ab initio molecular dynamics simulations. *J. Phys. Chem. C.* **126**, 12136–12149 (2022).
60. Moon, J., Lee, B., Cho, M. & Cho, K. Ab initio and kinetic Monte Carlo study of lithium diffusion in LiSi, $Li_{12}Si_7$, $Li_{13}Si_5$ and $Li_{15}Si4$. *J. Power Sources* **328**, 558–566 (2016).
61. Kvist, A. & Trolle, U. Self-diffusion and transport mechanisms in cubic lithium sulphate. *Z. f.ür. Naturforsch. A* **22**, 213–214 (1967).
62. Yu, M. & Trinkle, D. R. Accurate and efficient algorithm for Bader charge integration. *J. Chem. Phys.* **134**, 064111 (2011).
63. Van Der Ven, A., Ceder, G., Asta, M. & Tepesch, P. D. First-principles theory of ionic diffusion with nondilute carriers. *Phys. Rev. B* **64**, 184307 (2001).
64. Marcolongo, A. & Marzari, N. Ionic correlations and failure of Nernst-Einstein relation in solid-state electrolytes. *Phys. Rev. Mater.* **1**, 025402 (2017).
65. Yang, M., Raucci, U. & Parrinello, M. Reactant-induced dynamics of lithium imide surfaces during the ammonia decomposition process. *Nat. Catal.* **6**, 829–836 (2023).
66. Mambretti, F., Raucci, U., Yang, M. & Parrinello, M. How does structural disorder impact heterogeneous catalysts? The case of ammonia decomposition on non-stoichiometric lithium imide. *ACS Catal.* **14**, 1252–1256 (2024).
67. Kühne, T. D. et al. CP2K: An electronic structure and molecular dynamics software package - Quickstep: Efficient and accurate electronic structure calculations. *J. Chem. Phys.* **152**, 194103 (2020).
68. Perdew, J. P., Burke, K. & Ernzerhof, M. Generalized gradient approximation made simple. *Phys. Rev. Lett.* **77**, 3865–3868 (1996).
69. Goedecker, S., Teter, M. & Hutter, J. Separable dual-space Gaussian pseudopotentials. *Phys. Rev. B* **54**, 1703–1710 (1996).
70. Giannozzi, P. et al. Quantum espresso: a modular and open-source software project for quantum simulations of materials. *J. Phys.: Condens. Matter* **21**, 395502 (2009).
71. Giannozzi, P. et al. Advanced capabilities for materials modelling with quantum espresso. *J. Phys.: Condens. Matter* **29**, 465901 (2017).
72. Giannozzi, P. et al. Quantum ESPRESSO toward the exascale. *J. Chem. Phys.* **152**, 154105 (2020).

73. Raczkowski, D., Canning, A. & Wang, L. W. Thomas-Fermi charge mixing for obtaining self-consistency in density functional calculations. *Phys. Rev. B* **64**, 121101 (2001).
74. Wang, H., Zhang, L., Han, J. & E, W. DeePMD-kit: A deep learning package for many-body potential energy representation and molecular dynamics. *Comput. Phys. Comm.* **228**, 178–184 (2018).
75. Zeng, J. et al. DeePMD-kit v2: A software package for deep potential models. *J. Chem. Phys.* **159**, 054801 (2023).
76. Lu, D. et al. 86 PFLOPS deep potential molecular dynamics simulation of 100 million atoms with ab initio accuracy. *Comput. Phys. Comm.* **259**, 107624 (2021).
77. Zhang, L. et al. End-to-end symmetry preserving inter-atomic potential energy model for finite and extended systems https://arxiv.org/abs/1805.09003 (2018).
78. He, K., Zhang, X., Ren, S. & Sun, J. Deep residual learning for image recognition https://arxiv.org/abs/1512.03385 (2015).
79. Kingma, D. P. & Ba, J. Adam: a method for stochastic optimization https://arxiv.org/abs/1412.6980 (2014).
80. Thompson, A. P. et al. LAMMPS - a flexible simulation tool for particle-based materials modeling at the atomic, meso, and continuum scales. *Comp. Phys. Comm.* **271**, 108171 (2022).
81. Bussi, G., Donadio, D. & Parrinello, M. Canonical sampling through velocity rescaling. *J. Chem. Phys.* **126**, 014101 (2007).
82. Bonomi, M. et al. PLUMED: A portable plugin for free-energy calculations with molecular dynamics. *Comput. Phys. Commun.* **180**, 1961–1972 (2009).
83. Tribello, G. A., Bonomi, M., Branduardi, D., Camilloni, C. & Bussi, G. PLUMED 2: New feathers for an old bird. *Comput. Phys. Commun.* **185**, 604–613 (2014).
84. Himanen, L. et al. DScribe: Library of descriptors for machine learning in materials science. *Comput. Phys. Commun.* **247**, 106949 (2020).
85. Pedregosa, F. et al. Scikit-learn: Machine learning in Python. *J. Mach. Learn. Res.* **12**, 2825–2830 (2011).
86. Ester, M., Kriegel, H.-P., Sander, J. & Xu, X. A density-based algorithm for discovering clusters in large spatial databases with noise. *Proc. Second International Conference on Knowledge Discovery and Data Mining* 226–231 (1996).
87. Shi, Y., Ke, G., Chen, Z., Zheng, S. & Liu, T.-Y. Quantized Training of Gradient Boosting Decision Trees https://arxiv.org/abs/2207.09682 (2022).
88. Marcos-Alcalde, I., Setoain, J., Mendieta-Moreno, J. I., Mendieta, J. & Gómez-Puertas, P. MEPSA: minimum energy pathway analysis for energy landscapes. *Bioinformatics* **31**, 3853–3855 (2015).

Acknowledgements

We thank Axel Tosello Gardini for the suggestion and discussion about the use of unsupervised ML and SOAP descriptors. We acknowledge ISCRA (IsB29_NEXT-LIB) for awarding this project access to the LEONARDO supercomputer, owned by the EuroHPC Joint Undertaking, hosted by CINECA (Italy). E.C. acknowledges funding under the National Recovery and Resilience Plan (NRRP), Mission 4 Component 2 Investment 1.3 - Call for tender No. 1561 of 11.10.2022 of Ministero dell'Università e della Ricerca (MUR); funded by the European Union - NextGenerationEU.

Author contributions

P.D.A. conceived the study, curated the data, performed the formal analysis and investigation, developed the methodology and software, supervised the project, and wrote the original draft. U.R. and F.M. also contributed to the conceptualization, formal analysis, investigation, methodology, project administration, and supervision, while also writing and editing the manuscript. M.F., E.C., and P.A. reviewed and edited the manuscript, with E.C. and P.A. also acquiring funding and providing supervision. M.P. was involved in conceptualization, funding acquisition, methodology, project administration, and supervision. All authors reviewed the final manuscript.

Competing interests

The authors declare no competing interests.

Additional information

Supplementary information The online version contains supplementary material available at https://doi.org/10.1038/s41524-026-02132-8.

Correspondence and requests for materials should be addressed to Paolo De Angelis or Michele Parrinello.

Reprints and permissions information is available at http://www.nature.com/reprints

Publisher's note Springer Nature remains neutral with regard to jurisdictional claims in published maps and institutional affiliations.

Open Access This article is licensed under a Creative Commons Attribution-NonCommercial-NoDerivatives 4.0 International License, which permits any non-commercial use, sharing, distribution and reproduction in any medium or format, as long as you give appropriate credit to the original author(s) and the source, provide a link to the Creative Commons licence, and indicate if you modified the licensed material. You do not have permission under this licence to share adapted material derived from this article or parts of it. The images or other third party material in this article are included in the article's Creative Commons licence, unless indicated otherwise in a credit line to the material. If material is not included in the article's Creative Commons licence and your intended use is not permitted by statutory regulation or exceeds the permitted use, you will need to obtain permission directly from the copyright holder. To view a copy of this licence, visit http://creativecommons.org/licenses/by-nc-nd/4.0/.

© The Author(s) 2026